Nucleic Acids Research, 2025, **53**, gkaf152
https://doi.org/10.1093/nar/gkaf152
Molecular and Structural Biology

Spatiotemporal dynamics of protamine–DNA condensation revealed by high-speed atomic force microscopy

Goro Nishide[1], Keesiang Lim[2], Akiko Kobayashi[2], Yujia Qiu[3], Masaharu Hazawa[2,4], Toshio Ando[2], Yuki Okada[5,*], Richard W. Wong[1,2,3,4,*]

[1]Division of Nano Life Science in the Graduate School of Frontier Science Initiative, WISE Program for Nano-Precision Medicine, Science and Technology, Kanazawa University, Kanazawa, Ishikawa 920-1192, Japan
[2]WPI-Nano Life Science Institute, Kanazawa University, Kakuma-machi, Kanazawa, Ishikawa 920-1192, Japan
[3]Division of Nano Life Science in the Graduate School of Frontier Science Initiative, Kanazawa University, Kanazawa Ishikawa 920-1192, Japan
[4]Cell-Bionomics Research Unit, Institute for Frontier Science Initiative (INFINITI), Kanazawa University, Kakuma-machi, Kanazawa, Ishikawa 920-1192, Japan
[5]Institute for Quantitative Biosciences, The University of Tokyo, Tokyo113-0032, Japan

[*]To whom correspondence should be addressed. Email: rwong@staff.kanazawa-u.ac.jp
Correspondence may also be addressed to Yuki Okada. Email: ytokada@iqb.u-tokyo.ac.jp

Abstract

Protamines (PRMs) play a crucial role in sperm chromatin condensation, replacing histones to form nucleo–PRM structures, specifically PRM–DNA complexes. Despite their importance in reproduction, the detailed mechanisms underlying PRM-mediated DNA condensation have remained elusive. In this study, we employed high-speed atomic force microscopy (HS-AFM) to directly visualize the real-time binding dynamics of PRM to DNA under physiological conditions. Our HS-AFM observations reveal that PRM insertion initiating the formation of DNA coils. Further, we observed a heterogeneous spatial distribution of PRM-induced DNA looping. With continuous PRM addition, DNA progresses through a series of folding transitions, forming coiled-like structures that evolve into clockwise spirals, rod-shaped intermediates, and ultimately toroid-like nanostructures. Based on these real-time observations, we propose the CARD (Coil-Assembly-Rod-Doughnut) model to describe the stepwise process of toroid formation during DNA condensation. Our findings underscore the versatility of HS-AFM in capturing the spatiotemporal dynamics of PRM–DNA interactions and provide critical insights into the molecular mechanisms driving PRM-induced chromatin compaction. This study advances our understanding of sperm chromatin architecture and offers a framework for future research into chromatin organization, reproductive biology, and nucleic acid therapeutics.

Graphical abstract

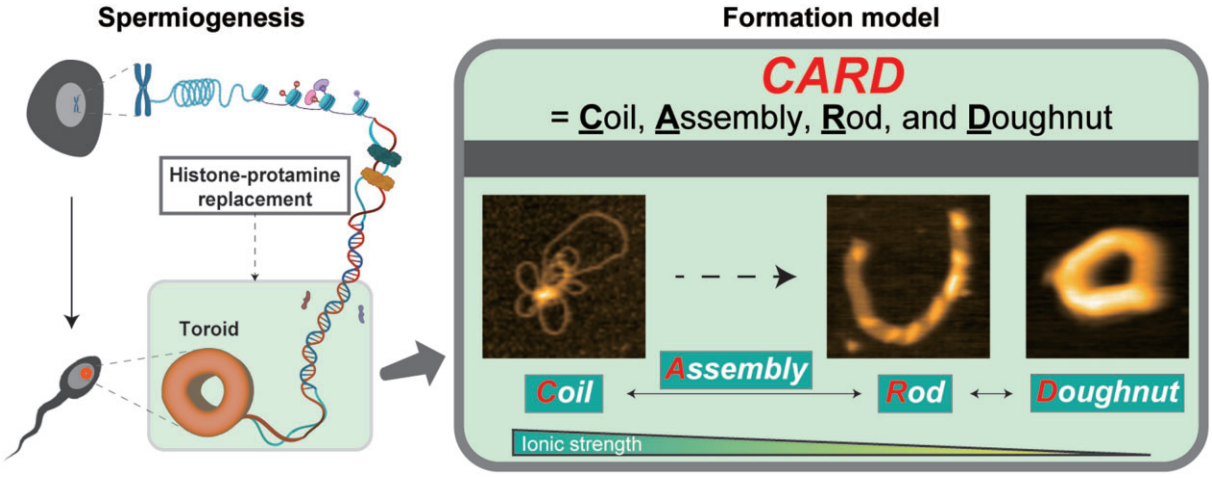

Received: September 12, 2024. **Revised:** February 6, 2025. **Editorial Decision:** February 11, 2025. **Accepted:** February 21, 2025

Introduction

Sperm cells in mammals are equipped with incredibly complex structures and functions, which allow them to carry out the process of fertilization, which is essential for the continuation of life [1, 2]. There are three stages of spermatogenesis: mitotic, meiotic, and post-meiotic. In the post-meiotic stage, histones in germ cells are replaced with protamines (PRMs) to acquire the physical protection of their DNA for fertilization. As a result, over 90% of histones in mature sperm cells are substituted with PRMs, PRM1 and PRM2, in most mammals including mice and humans [3].

PRMs are basic, positively charged proteins characterized by the arginine- and cysteine-rich sequences that bind to negatively charged phosphate backbone of DNA and form intra- and inter-molecular disulfide bonds that ensure the highly condensed chromatin. After PRM interacts with DNA, DNA loops into toroids, and sperm chromatin becomes very dense [4]. These short (30–50 residues), positively charged, inherently disordered proteins condense genomic DNA 10–20 times more than in somatic cells [5]. Nuclear cohesiveness is one of the most notable characteristics of this system. Intense compression shields sperm DNA from harm and aids in transporting it to the ooplasm. Over the last 30 years, various imaging methods, such as transmission electron microscopy (TEM), atomic force microscopy (AFM) [6–9], and fluorescence microscopy [10], have been employed to study the structures of DNA when condensed by PRM. Hud *et al.* suggested that PRM condenses sperm DNA into toroids with a capacity of up to 60 kb based on TEM and AFM imaging [9]. Recent AFM research on shorter DNA has identified many forms such as single loops [7], numerous loops originating from a central point, and stacks of loops [6]. Single-molecule fluorescence imaging has demonstrated that DNA may be condensed to nearly zero length when completely coated with PRM [10]. These efficient nucleic acid condensation effects by PRM have been continuously studied for many years because of their potential application in gene delivery therapy and nucleic acid vaccines.

Contrary to the remarkable DNA condensation effects seen *in vitro*, although it is still controversial [11, 12], the 3D chromatin architecture of mouse sperm closely resembles that of somatic cells, as indicated by high-throughput chromosomal conformation capture data [3, 13], including the presence of topologically associating domains and compartments. Thus, it is uncertain if PRM functions just at a local level similar to histones, or if it also contributes to the higher-level organizing of sperm chromatin associated with genome-wide transcriptional inactivation [14]. On the other hand, the specific mechanism (the manner in which PRM aggregates DNA to form dense toroidal structures) is not yet completely known. Furthermore, sperm need to adapt to various external environments as they are released from the testis into the epididymis and the uterus. Therefore, understanding the behavior of sperm chromatin in response to these external environments [15], such as ionic environments, is extremely important in consideration of the increasing demand for assisted reproductive technology in recent years [16].

Because of this, we decided to perform a study utilizing high-speed atomic force microscopy (HS-AFM) [17, 18], which is capable of capturing the dynamics of biomolecules at the nanoscale and in sub-seconds. HS-AFM is a distinctive method in dynamic structural biology that allows for the observation of individual molecules in motion [19]. We have shown that HS-AFM is capable of providing real-time imaging of the organelles such nuclear pore complexes [20–22] and small extracellular vesicles (sEVs) [23] at a nanoscale resolution, dynamic conformational changes in viral fusion proteins [24–27], as well as interactions between histone H2A and DNA [28].

In this study, we employed HS-AFM to systematically investigate the DNA compaction process induced by PRMs on supported lipid bilayers. Our findings reveal that PRM triggers the initiation of coil formation. Notably, HS-AFM imaging showed a heterogeneous spatial distribution of DNA loops induced by PRM binding. Furthermore, as PRMs were continuously introduced, DNA underwent a sequence of structural transitions, beginning with the formation of coiled-like configurations, which progressively developed into clockwise spirals. These spirals subsequently condensed into rod-like structures and ultimately formed toroid-shaped nanoscopic assemblies. Our analysis demonstrates that the kinetics and compaction dynamics of these various supramolecular structures—loops, spirals, and coiled-like forms—differ significantly. Additionally, our experiments suggest that sufficiently large spirals can transition into regular rolls and toroid formation. We hypothesize that the lateral association of PRMs with these rolls, leading to toroid thickening, may represent a mechanism for modulating the mechanical properties of the polymer as the supramolecular DNA structures undergo compaction. Based on these observations, we propose the CARD (Coil-Assembly-Rod-Doughnut) model to describe the process of toroid formation, thereby providing deeper insights into the critical role of PRMs in DNA compaction.

Materials and methods

Materials

1,6-Hexanediol (1,6-HD), fish PRM (PRM), and magnesium chloride were all sourced from Tokyo Chemical Industry Co., Ltd. (Tokyo, Japan).

Plasmids

The pGEM-3z/601 plasmid was obtained from Addgene (Watertown, MA). Linearized double-stranded DNA (dsDNA) fragments (2716 bp) were prepared as previously described [5]. λDNA was obtained from Nippon Gene Material Co., Ltd. (Tokyo, Japan).

In silico analysis of PRM protein properties

The net charge of PRM protein at pH 7.4 was determined using the Protpi webserver (https://www.protpi.ch/). Hydropathicity was assessed using the Eisenberg scale available through the Expasy ProtScale webserver (https://web.expasy.org/protscale/). Intrinsically disordered regions (IDRs) within the PRM protein were predicted using multiple IDR predictors, including the IUPRED series (long and short), PONDR series (VL3, VLXT, VSL2, and FIT), PrDOS, and DISOPRED, following methods previously described [5]. The outputs from these eight IDR predictors were consolidated into a single graph.

AlphaFold3 prediction

The amino acid sequences of PRM and the corresponding DNA were submitted to the AlphaFold3 prediction pipeline to generate a 3D structural model and binding predictions. The AlphaFold Server (https://golgi.sandbox.google.com/) was used for this purpose. A comprehensive template search was conducted using the Protein Data Bank (PDB) to identify homologous structures as references. The deep learning model predicted inter-residue distances and angles, which were further refined through iterative optimization to enhance accuracy. The final structural model was generated in PDB format, providing a detailed representation of the PRM–DNA interaction.

HS-AFM imaging

HS-AFM images were acquired using a custom-built tapping mode HS-AFM, as detailed in previous studies [5]. Small cantilevers (BL-AC10-DS-A2 from Olympus, Tokyo, Japan; USC-F1.2-k0.15 and USC-F1.5-k0.6 from NanoWorld, Neuchâtel, Switzerland) with spring constants (k) of 0.1, 0.15, and 0.6 N/m and resonance frequencies (f) of 1.5, 1.2, and 1.5 MHz were used. To enhance image quality, amorphous carbon was deposited on the cantilever tip using electron-beam deposition with a field emission scanning electron microscope (ELS-7500, Elionix Inc., Tokyo, Japan). A laser beam (670 nm wavelength) was focused on the electron beam deposited (EBD)-processed cantilever tip using a 20×-objective lens (CFI S Plan Fluor ELWD, Nikon, Tokyo, Japan). The cantilever's dynamic deflection was detected by a position-sensing two-segmented PIN photodiode. To optimize tip-sample interaction force, the free oscillation amplitude of the cantilever (A0) was adjusted to 1.5–2.5 nm, with the set-point tuned to 80%–90% of the free amplitude. A glass stage coated with muscovite mica layers (~0.1 mm total thickness) was affixed to the HS-AFM scanner.

For scanning the native conformation of PRM protein, the sample was first diluted in a scanning buffer (10 mM Tris–HCl, 2 mM $MgCl_2$, pH 7.4) to a concentration of 50 ng/μl. The sample was then loaded onto bare mica (negatively charged) and incubated for 5 min. Following incubation, the substrate was rinsed with scanning buffer to remove unbound PRM protein before proceeding with HS-AFM scanning.

To investigate the role of electrostatic attraction or hydrophobic interaction in PRM aggregation in real-time, 100 ng/μl PRM protein was first loaded onto bare mica (negatively charged), and the concentration of NaCl or 1,6-HD was adjusted to 1.5 M or 15% during HS-AFM scanning.

For PRM–DNA aggregation scanning, a premix sample was prepared and incubated on ice for 5 min before HS-AFM scanning. The premix contained varying concentrations of PRM, DNA, and buffer components ($MgCl_2$). After incubation, the premix was loaded onto bare mica (negatively charged), incubated for 5 min, and rinsed with scanning buffer to remove unbound PRM and DNA before HS-AFM scanning. To explore the role of electrostatic attraction or hydrophobic interaction in PRM–DNA aggregation in real-time, the aggregations were first loaded onto bare mica (negatively charged), and the NaCl or 1,6-HD concentration was adjusted to 500 mM or 15% during HS-AFM scanning. The NaCl/$MgCl_2$ concentration was adjusted by manually exchanging the buffer in the AFM observation chamber with a buffer containing the desired NaCl/$MgCl_2$ concentration during the condensate observation. The effect of divalent ions on PRM–DNA aggregation was examined by loading the premix onto bare mica (negatively charged) and adjusting the $MgCl_2$ concentration to 500 mM during HS-AFM scanning.

To capture the real-time process of DNA compaction by PRM, DNA was first loaded and incubated on bare mica (negatively charged), lipid-coated mica (positively charged) for 5 min. For cationic lipid bilayer substrate preparation, a mixture containing 0.2 mg/ml DPPC/DPTAP/biotin-cap-DPPE (90:5:5 mass ratio) in 10 mM $MgCl_2$ was sonicated for 5 min in a bath sonicator (7-5027-01, AS ONE, Osaka, Japan) before being deposited onto the bare mica surface, creating a positively charged surface to minimize DNA–substrate interactions. The substrate was rinsed with scanning buffer to remove unbound DNA and debris before HS-AFM scanning. During scanning, the PRM concentration in the chamber was adjusted by replacing the imaging buffer with a solution containing PRM.

For scanning spermidine–DNA aggregations, a premix sample was prepared and incubated on ice for 5 min before HS-AFM scanning. The premix contained varying concentrations of PRM, DNA, spermidine, and buffer components ($MgCl_2$). After incubation, the premix was loaded onto bare mica (negatively charged), incubated for 5 min, and rinsed with scanning buffer to remove unbound PRM and DNA before HS-AFM scanning.

All experiments were repeated at least three times to ensure reproducibility.

HS-AFM image processing and analysis

All HS-AFM images were processed and analyzed using ImageJ software (https://imagej.net/ij/download.html). A first-order polynomial fit in both x- and y-directions was applied, followed by convolution with a Gaussian smoothing function using the "Gaussian Blur" plugin to enhance image quality. Spatial parameters, including cross-sectional height, were measured using the same software. The processed image sequences were saved as videos (AVI format) and then arranged, edited, and compiled using Adobe Creative Cloud (https://www.adobe.com/creativecloud.html).

To evaluate aggregation, the area surrounding the aggregations or scattered particles in each sequential frame was measured. A box was drawn around the aggregations and all scattered particles, and the area of that box was calculated.

Statistical analysis

Graphs were generated using R software (R Development Core Team). Comparative analyses were performed using SPSS version 28 (IBM Corp., NY, USA). Independent samples were compared using either the Student's *t*-test or Mann–Whitney U test. Related samples (before and after) were compared using either the paired *t*-test or Wilcoxon-signed rank test. Statistical significance was set at $^{*}P < .05$, $^{**}P < .01$.

Results

Direct observation of PRM–DNA complex compaction kinetics using HS-AFM

To investigate the structural dynamics of PRM-induced DNA condensation, HS-AFM was employed to capture the real-time compaction of PRM–DNA complexes on mica sur-

faces. The negatively charged surface of bare mica facilitates the adsorption of PRMs and PRM–DNA complexes, while free PRMs attached to the surface reduce excessive adsorption forces, preserving the structural integrity of the complexes and ensuring they remain intact during scanning (Figs 1 and 2, Supplementary Figs S1–S3, and Supplementary Movies S1–S7).

The experimental setup (Fig. 1A) was complemented by AlphaFold3 predictions to model the structural interactions, though these predictions do not currently simulate real-time condensation dynamics. Real-time HS-AFM imaging provided direct evidence of the attractive forces between PRM and adjacent DNA strands during the condensation process. The observed movement and reorientation of the PRM–DNA complex on the surface reflect the dynamic nature of electrostatic interactions. The flexibility and reorientation suggest an electrostatically mediated interaction between the PRM–DNA complex and the mica surface, rather than a visualization of force itself. The electrostatic interactions between the positively charged PRM and negatively charged DNA facilitated this hierarchical condensation, ultimately culminating in toroidal structures.

Interestingly, the addition of the liquid-liquid phase separation (LLPS) inhibitor 1,6-HD at concentrations up to 15% did not induce decompaction (Supplementary Figs S1E and S3, and Supplementary Movie S1), suggesting that PRM–DNA interactions are not phase separation-dependent. Instead, the PRM-induced "beads-on-a-string" structures observed during scanning remained dynamic, highlighting the flexibility and mobility of PRM–DNA complexes (Fig. 1B and Supplementary Movie S2). These dynamics are essential for the stepwise condensation process, allowing the complexes to efficiently rearrange and transition between intermediate structures, ultimately forming toroidal aggregates.

Unlike hydrophobicity-driven condensates characteristic of LLPS, PRM–DNA structures dissolve exclusively under high ionic strength, as demonstrated by NaCl and Mg^{2+} treatments. This finding emphasizes the dominance of ionic interactions in regulating the stability and condensation of PRM–DNA complexes.

The use of 1,6-HD, a well-established tool for disrupting LLPS-driven assemblies, further confirmed the absence of hydrophobic contributions to PRM–DNA compaction or decompaction. Together, these results highlight the critical role of electrostatic forces in both the formation and dissolution of PRM–DNA complexes, while demonstrating the reversibility and adaptability of these structures under varying ionic conditions.

HS-AFM imaging captured a diverse array of PRM–DNA complexes, including Coil (9.1%), Rod (85.3%), and Doughnut (5.6%) structures when using 2.7 kbp DNA ($n = 143$). With longer DNA molecules (50.0 kbp, $n = 234$), the distribution shifted to Coil (1.3%), Rod (74.8%), and Doughnut (23.9%) conformations, as shown in Fig. 1C and D. These findings highlight the impact of DNA length on the resulting conformations.

Sequential imaging further revealed a stepwise transition from initial looping to compaction upon PRM addition (up to 1.7 ng/μl) (Fig. 1E and Supplementary Movie S3). PRM binding induced the formation of compact structures with a characteristic height of ∼6 nm (Fig. 1E). DNA molecules immobilized on mica (mean length = 924.5 nm) were examined under varying PRM concentrations (up to 100 ng/μl) (Supplementary Fig. S3). Complete DNA condensation was observed at concentrations exceeding 1 ng/μl, consistent with previous studies on long DNA molecules (∼50 μm) [10]. In the absence of PRM, the DNA remained linear on the mica surface, whereas PRM addition induced DNA folding and aggregation, mirroring prior AFM findings [7, 8, 29].

These results underscore the versatility of PRM in inducing a range of DNA conformations, from loosely organized loops to fully compacted toroids. HS-AFM provided direct, real-time evidence of the dynamic and hierarchical nature of DNA condensation, revealing the nanoscale structural transitions that drive toroid formation.

Influence of electrostatic and ionic strength on PRM–DNA compaction

To investigate the role of ionic concentration in PRM-induced DNA compaction, we applied HS-AFM to capture the real-time dynamics of PRM–DNA complex formation and dissolution. Bare mica was used as the initial substrate, and imaging began in 10 mM Tris–HCl buffer before sequentially introducing PRM and DNA. The addition of PRM induced the formation and enlargement of PRM–DNA aggregates, followed by controlled dissolution when the buffer was replaced with increasing concentrations of NaCl. Sequential HS-AFM imaging revealed stepwise disassembly of rod- and toroid-shaped PRM–DNA complexes, with complete dissolution observed at 500 mM NaCl, indicating that electrostatic interactions are central to the reversible formation and dissociation of these structures (Fig. 2A and B and Supplementary Movies S4 and S5).

Systematic analysis of the condensation area and height ratios before (t = 0) and after (t = 300 s) salt addition (Fig. 2C and D) revealed significant reductions in PRM–DNA complex density. This was visually supported by the shift in color intensity, from bright (compact) to dark (dissociated), confirming that both rod and toroid structures disassemble under high-salt conditions.

Beyond monovalent ions, we examined the effect of divalent ions such as Mg^{2+} on PRM–DNA compaction, given their reported dual role in nucleosome condensation and nucleo–PRM decondensation [30, 31]. Sequential HS-AFM imaging demonstrated that increasing Mg^{2+} concentrations (up to 500 mM) initially enhanced DNA condensation but ultimately led to the destabilization and partial disintegration of the globular structures beyond a critical threshold (Fig. 2E, Supplementary Fig. S4, and Supplementary Movies S6 and S7). These observations suggest that higher Mg^{2+} concentrations weaken electrostatic interactions due to charge screening, creating an unstable intermediate state characterized by increased DNA flexibility and partial uncoiling.

Scatter plots from three independent examples (Fig. 2F) showed a steady increase in the real-time area of PRM–DNA complexes with the addition of $MgCl_2$, reaching a maximum at 500 mM. This pattern indicates progressive dissociation of the complexes. Comparative analysis of PRM–DNA areas under different ionic strengths (Fig. 2G) supports the hypothesis that high Mg^{2+} concentrations reduce electrostatic interactions between DNA segments, resulting in loosely organized network structures.

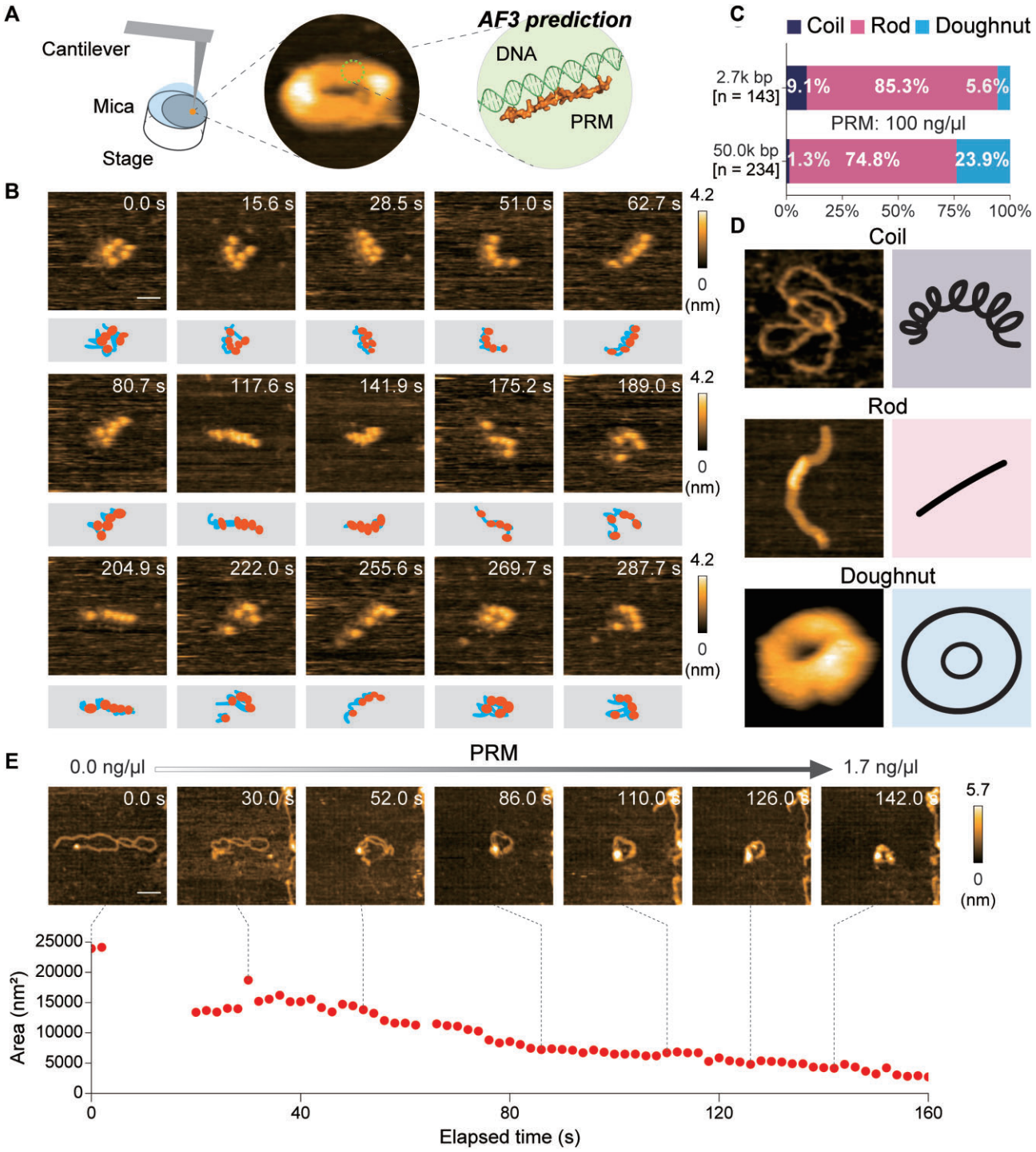

Figure 1. Real-time HS-AFM imaging of PRM–DNA complexes and their dynamic condensation process. (**A**) Schematic of the HS-AFM setup used to visualize the PRM–DNA interaction, alongside AlphaFold3 predictions illustrating the interaction between PRM and DNA. (**B**) HS-AFM captures real-time dynamics of PRM-induced DNA condensation on bare mica. The sequential images show PRM–DNA complexes transitioning from loose aggregates into more compact structures, demonstrating the highly dynamic nature of PRM–DNA binding. The rod structures observed are prone to transformation into toroids while maintaining their overall stability (scale bar: 20 nm). (**C**, **D**) HS-AFM images illustrating a variety of PRM–DNA aggregates, including coiled-like, rod-shaped, and toroidal (Doughnut) structures, with distinct distributions depending on DNA length. Using 2.7k bp DNA, Coil (9.1%), Rod (85.3%), and Doughnut (5.6%) structures were observed ($n = 143$). In contrast, for 50.0k bp DNA, the distribution shifts to Coil (1.3%), Rod (74.8%), and Doughnut (23.9%) ($n = 234$). (**E**) Sequential HS-AFM images show the progression of DNA looping and condensation following PRM addition (up to 1.7 ng/μl), demonstrating the stepwise compaction process on bare mica. The plot of aggregate area (nm^2) versus elapsed time (s) provides systematic support for the concentration-dependent nature of DNA condensation by PRM.

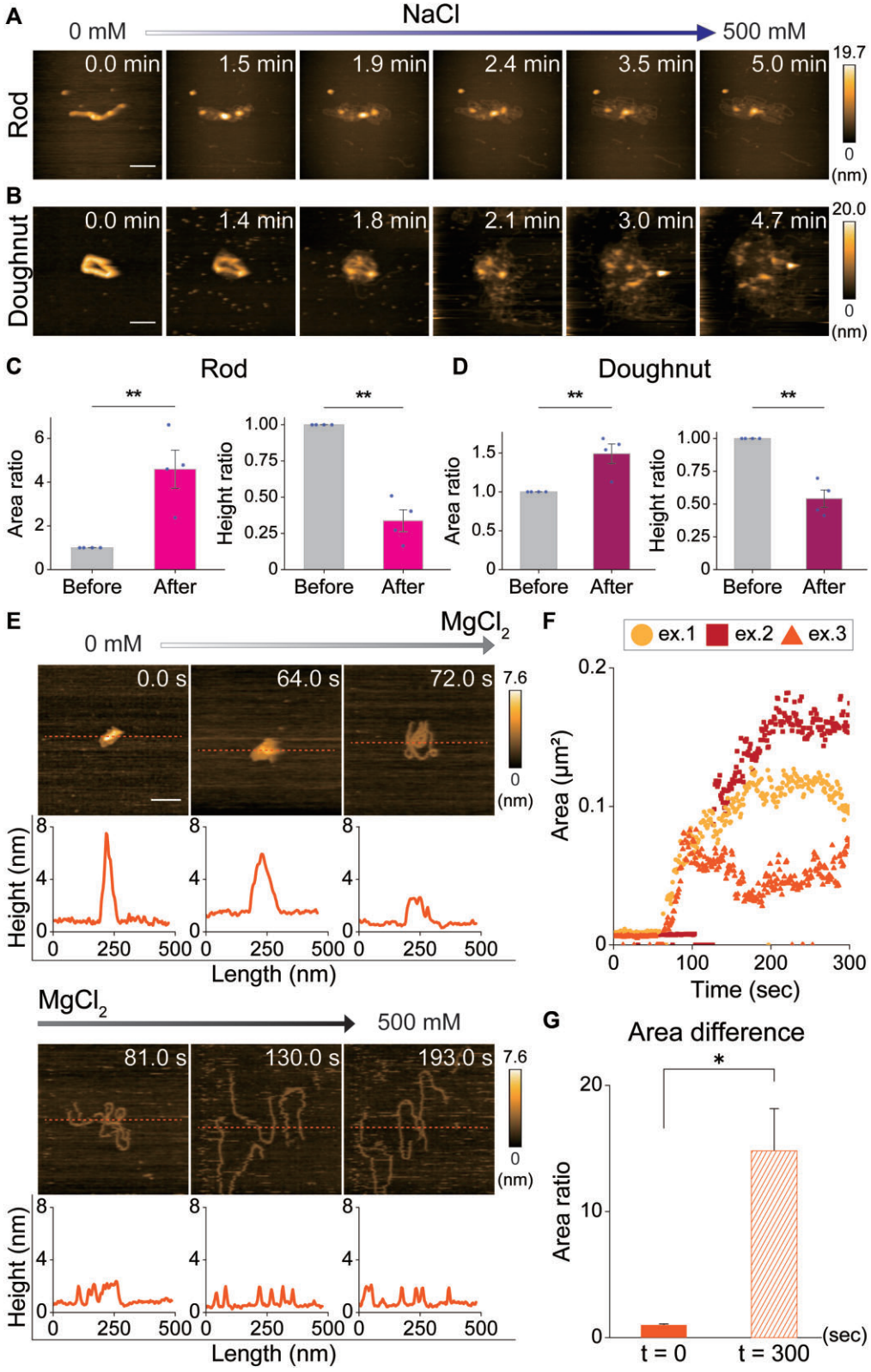

Figure 2. Dissolution of PRM–DNA complexes under varying ionic strength conditions observed via HS-AFM. (**A**, **B**) Sequential HS-AFM images capture the gradual dissolution of PRM–DNA Rod and Doughnut structures on bare mica upon increasing the ionic strength using NaCl (up to 500 mM). The images show that high ionic conditions disrupt the stability of these complexes, leading to their disassembly (scale bars: 200 nm and 140 nm, respectively). (**C**, **D**) Bar graphs depicting the ratio of DNA condensation area and height before (t = 0) and after (t = 300 s) NaCl addition, highlighting significant reductions in both parameters under high ionic strength [mean ± standard error of the mean (SEM), $n = 4$, $^{**}P < .01$, two-tailed paired *t*-test]. (**E**) HS-AFM images showing the dissolution of PRM–DNA complexes on bare mica upon the introduction of divalent magnesium ions ($MgCl_2$) at increasing concentrations (up to 500 mM), further indicating the ionic sensitivity of these aggregates (scale bar: 100 nm). (**F**) Scatter plots illustrating the real-time changes in PRM–DNA complex size as Mg^{2+} concentrations rise, demonstrating that complex dissociation accelerates as the ionic strength increases. (**G**) Comparative analysis of the size of PRM–DNA complexes under varying ionic strengths, with statistical significance indicated for changes in complex size at higher concentrations of $MgCl_2$ (mean ± SEM, $n = 3$, $^{*}P < .05$, two-tailed paired *t*-test).

Rapid conformational changes in DNA looping by PRM: from coiled-like loops to toroid patterns observed via HS-AFM

Previous studies, including our own, have demonstrated that the topology of dsDNA on various surfaces, such as (3-aminopropyl)triethoxysilane or poly-l-lysine, depends heavily on surface adsorption forces. Under conditions of zero ionic strength, plasmids experience strong electrostatic interactions with positively charged substrates, leading to compaction, folding, and immobilization on mica. Conversely, high ionic strength reduces these adsorption forces, allowing plasmids to extend and self-organize into plectonemic supercoils. Segmental mobility of plasmids is observed on surfaces with reduced adsorption strength, where interactions are weaker.

To minimize artificial coiling and preserve DNA mobility, we utilized a cationic lipid bilayer substrate composed of DPPC/DPTAP/biotin-cap-DPPE (90:5:5 mass ratio). DNA immobilized on fluidic cationic lipid-coated mica (positively charged) exhibited significantly greater dynamic rearrangements, whereas only limited movement was observed on the nonfluidic bare mica (negatively charged) surface. Linearized 2.7k bp DNA scanned in neutral physiological buffer without added salt appeared as a homogeneous thread with an average thickness of 9.28 ± 0.22 nm and a height of 1.73 ± 0.03 nm (n = 74). Upon interaction with PRM on the cationic lipid bilayer, DNA rapidly transitioned from extended linear forms to compacted supercoils, resembling "rod" configurations (Fig. 3A and B, Supplementary Figs S5 and S6, and Supplementary Movies S8–S11).

HS-AFM imaging enabled us to document the entire condensation process. We observed the progression of DNA topology through distinct conformational states:

- Loop formation: DNA initially forms looping structures upon PRM binding;
- Coiled configuration: These loops transition into coiled-like conformations with enhanced compaction;
- Twisting and compaction: The DNA undergoes increased twisting, leading to further compaction and structural organization; and
- Rod formation: The final stage results in highly condensed rod-shaped aggregates resembling toroids. These rapid conformational transitions were characterized by dynamic changes in the DNA's physical dimensions. Localized regions of DNA temporarily exhibited nearly double their original height during intermediate stages before reverting and twisting into rod-like formations (Fig. 3C–F).

While toroid formation is observed in bulk conditions, the final transition from rod-shaped intermediates to toroids could not be directly visualized in our HS-AFM setup, likely due to repulsive forces between the cationic lipid substrate and the positively charged PRM–DNA complexes. This highlights a technical constraint of surface-based imaging for studying late-stage compaction.

As the PRM concentration increased, the DNA transitioned progressively from its extended coil state to more compact forms. This transition followed a stepwise trajectory through intermediate entanglements, ultimately leading to stable rod-like aggregates. The ability of PRM to drive this hierarchical compaction process underscores its critical role in facilitating DNA condensation. To validate the generality of this compaction mechanism, we conducted comparative experiments using spermidine (3+) under low-salt conditions. Spermidine-treated DNA exhibited similar rod-like condensation and toroid formation (Supplementary Fig. S7 and Supplementary Movies S12 and S13). However, spermidine-induced transitions displayed a unique feature: increasing salt concentrations led to DNA unfolding into a coil state, with a monotonic response to ionic strength changes. This contrasts with the PRM-induced process, which proceeds through a distinct series of hierarchical intermediate states.

Based on these findings, we propose the CARD model (Coil, Assembly, Rod, and Doughnut) as a hierarchical framework to describe the stepwise organization of PRM-induced DNA compaction. Our real-time HS-AFM imaging captured sequential transitions in DNA topology, providing direct visual evidence of the dynamic and reversible nature of the condensation process. Each stage of the CARD model is supported by high-resolution HS-AFM images, highlighting the critical role of PRM in initiating, stabilizing, and maintaining DNA compaction. The reversible transitions, indicated by arrows in the model, underscore the delicate interplay between PRM binding and environmental factors such as ionic strength (Fig. 4). Furthermore, our results suggest that the uniformity of the toroidal structures' inner and outer diameters, as observed in Supplementary Fig. S8, ensures a robust and consistent packaging system, despite variations in intermediate configurations.

To further validate the CARD model, we performed reverse disassembly experiments to visualize the sequential events in the opposite direction. By introducing 400 mM NaCl, we successfully induced the gradual decondensation of toroid/doughnut-shaped structures, which transitioned back into rod-shaped intermediates and ultimately into coiled-like conformations (Supplementary Fig. S9 and Supplementary Movie S14). Altogether, these findings provide compelling evidence supporting the reversibility of the condensation process and strengthen the robustness of the CARD model.

These findings also illustrate the close relationship between DNA conformational changes and PRM addition, highlighting a stepwise compaction mechanism. The process begins with loosely organized coiled-like structures, progresses through entanglement and twisting, and culminates in highly condensed rod-shaped formations. This hierarchical organization not only reflects the critical role of PRM in DNA condensation but also provides insights into the dynamic interplay between DNA and PRM under physiological conditions.

Discussion

In this paper, using HS-AFM, we captured the dynamic process of PRM-induced DNA condensation and proposed the CARD model (Coil, Assembly, Rod, and Doughnut) as a framework for understanding its hierarchical organization. The stepwise transitions include: 1. **C**oiled, loop formation and configuration → 2. **A**ssembly and compaction → 3. **R**od formation→ 4. **D**oughnut formation (Figs 1–4).

At higher PRM concentrations, DNA progressively compacts into stable rod-like and toroidal structures. Comparative experiments with spermidine confirmed a similar conden-

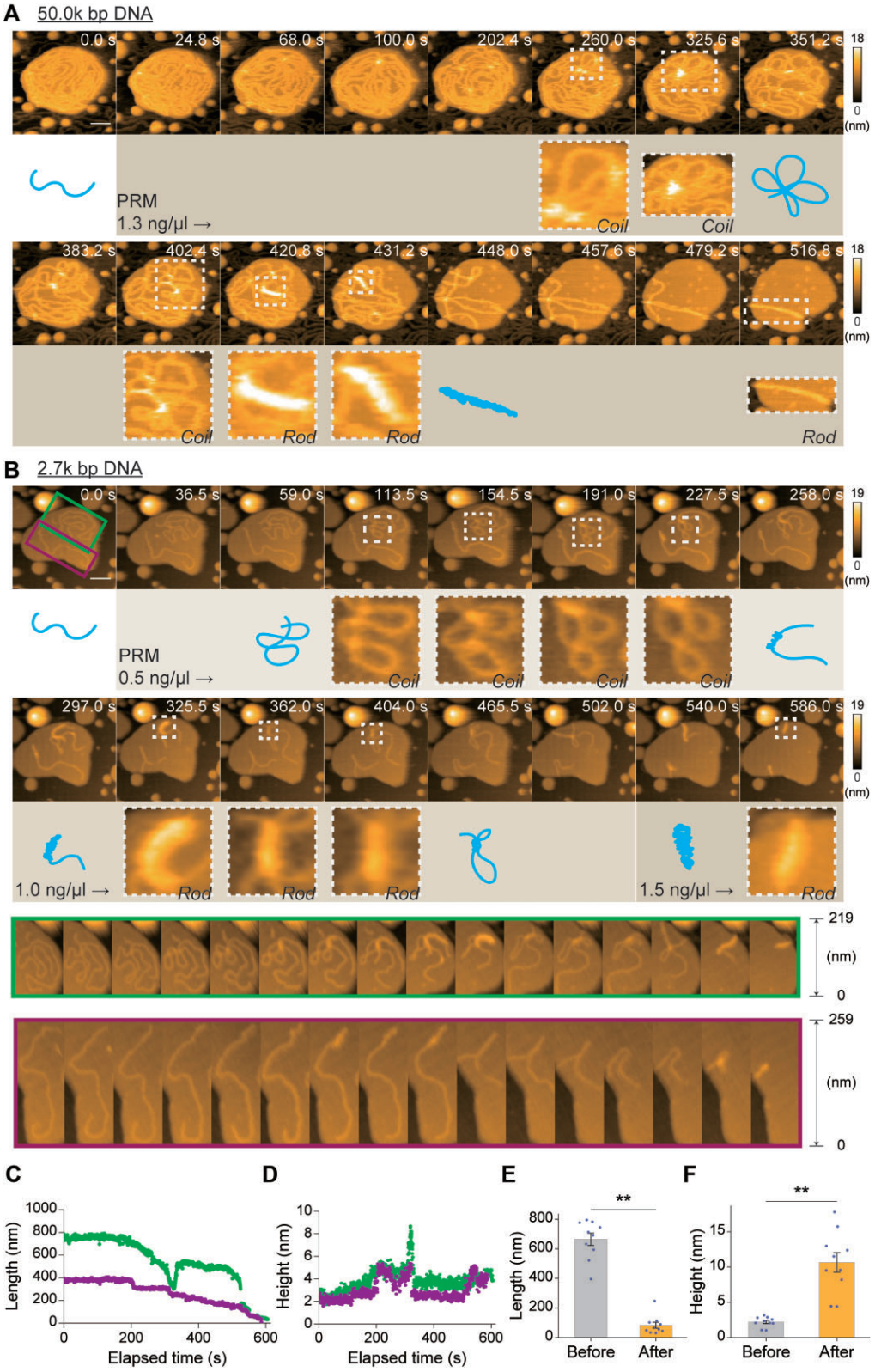

Figure 3. Sequential HS-AFM images capturing the PRM-induced DNA compaction process on a lipid bilayer. (**A**, **B**) Real-time HS-AFM images show the progression of (**A**) 50.0 kbp and (**B**) 2.7 kbp DNA condensation upon PRM addition on lipid-coated mica. DNA initially adopts an extended conformation that transitions into coiled-like looped structures, followed by the formation of rod-shaped aggregates as PRM concentration increases (scale bar: 70 and 100 nm, respectively). (**C**, **D**) Systematic analysis of the changes in DNA aggregate length and height over time in response to increasing PRM concentrations, showing a reduction in length and an increase in height as compaction proceeds. (**E**, **F**) Bar graphs comparing the length and height of DNA aggregates before (t = 0) and after (t = 600 s) PRM addition. The data demonstrate significant compaction, with a marked reduction in aggregate length and a concurrent increase in height (mean ± SEM, $n = 10$, $^{**}P < .01$, two-tailed paired *t*-test). This figure highlights the dynamic structural changes that occur during PRM-induced DNA condensation, supporting the proposed mechanism of stepwise compaction from looped intermediates to rod-like aggregates. These findings provide critical insights into the molecular basis of PRM–DNA interactions.

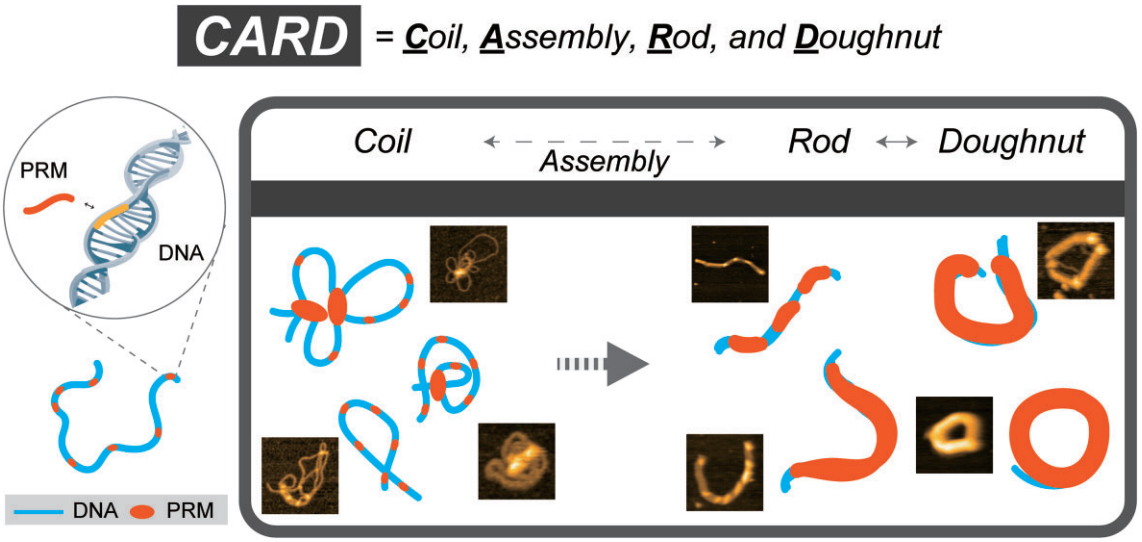

Figure 4. Proposed CARD model of PRM-induced DNA condensation. This graph illustrates the various stages of DNA condensation mediated by PRMs, as observed by HS-AFM. 1. Coil stage: • The DNA is in a loosely organized, flexible condition marked by scattered PRM binding. • The structure exhibits minimal compaction, displaying recognizable loops and irregular shapes. 2. Assembly stage: • PRMs initiate aggregation along the DNA backbone, facilitating the formation of intermediate, more structured configurations. The interactions are mostly regulated by electrostatic forces, resulting in the conversion of DNA into semi-condensed forms. 3. Rod stage: • The DNA–PRM complex experiences further compaction into rod-like forms. • These linear and elongated structures demonstrate heightened organization and density. 4. Doughnut (toroid) stage: • The final stage produces highly compacted toroidal structures, enhancing compaction and stability. • These doughnut-shaped forms are indicative of fully condensed DNA–PRM complexes.

sation process, though the unfolding response to salt differed from PRM-treated DNA.

To validate the CARD model, reverse disassembly experiments using 400 mM NaCl demonstrated the gradual decondensation of toroidal structures back into rod and coiled conformations, confirming the dynamic and reversible nature of the condensation process. These findings emphasize the critical role of PRM and electrostatic forces in DNA compaction and highlight the robustness of the CARD model as a framework for describing this process (Supplementary Fig. S9 and Supplementary Movie S14).

The compaction and packaging of DNA within sperm nuclei are fundamental for ensuring the accurate and safe transmission of the genome to the next generation. Through the use of HS-AFM with unparalleled spatiotemporal resolution, we captured the dynamic process of DNA condensation mediated by PRM. This process begins with coiled-like structures and progresses through intermediate conformations, such as sausage- and headphone-like forms, ultimately culminating in highly compact doughnut-shaped toroids. This study reveals that DNA condensation is driven by PRM–DNA interactions and modulated by ionic strength, underscoring the critical influence of PRM concentration and electrostatic forces in achieving proper chromatin compaction in mammalian sperm.

Our HS-AFM observations demonstrated that PRM binding induces local destabilization of DNA structure, initiating the formation of coiled-like loops through intercalation between DNA bases. Moreover, we observed a heterogeneous spatial distribution in PRM-induced DNA looping, suggesting that condensation occurs in a nonuniform, stepwise manner. Remarkably, with continuous PRM addition, DNA underwent sequential conformational changes, evolving from coiled-like loops to clockwise spirals and tie-shaped intermediates before fully condensing into toroid-like nanostructures. These findings provide crucial insights into the molecular mechanisms of PRM–DNA interactions, supporting a stepwise compaction pathway that transitions through looped and entangled intermediates before achieving rod-shaped aggregates and final toroidal structures.

A notable feature of the CARD model (Fig. 4) is its ability to bridge the gap between intermediate conformations and fully condensed toroids, which are essential for chromatin stability and genome protection in sperm. This cohesive understanding not only sheds light on the molecular steps of chromatin organization during spermiogenesis but also highlights the critical role of electrostatic forces in driving and regulating DNA condensation.

Beyond sperm biology, the CARD model offers broader implications for chromatin biology, particularly in understanding how variations in PRM concentration, mutations, or ionic environments may impact chromatin organization and male fertility. These insights have significant translational potential, providing a foundation for developing targeted therapies to address male infertility and refine assisted reproductive technologies. For example, perturbations in PRM–DNA interactions may lead to improper genome packaging, increasing susceptibility to genetic instability or infertility. Understanding these mechanisms could lead to novel approaches for modulating chromatin condensation in therapeutic contexts.

The application of HS-AFM in this study also highlights its unique capacity to capture nanoscale biomolecular dynamics in real time, providing insights that static imaging techniques cannot achieve. By enabling the visualization of DNA conformational changes with high spatiotemporal resolution, HS-AFM revealed the stepwise maturation process of DNA condensation, from initial coiling to final toroidal configura-

tions. These observations offer an unprecedented view of the dynamic interplay between PRM and DNA, advancing our understanding of chromatin dynamics and its regulation.

In conclusion, our findings elucidate the molecular mechanisms underlying PRM-induced DNA condensation, establishing the CARD model as a significant advance in chromatin biology. This model provides a detailed roadmap for understanding DNA compaction, emphasizing the stepwise transitions through distinct conformations that are critical for chromatin organization and stability. By integrating insights into chromatin condensation during spermiogenesis, this study opens new avenues for exploring genome protection mechanisms, fertility regulation, and chromatin dynamics in broader biological contexts. These discoveries provide a foundation for future investigations into the molecular pathways governing chromatin organization and their implications for reproductive health and disease.

Acknowledgements

We thank Prof. Noriyuki Kodera for providing the cationic lipid substrate, and we are grateful to all members of Richard Wong laboratory for their involvement. This work was supported by The World Premier International Research Center Initiative (WPI). This work was also supported by WISE Program for Nano-Precision Medicine, Science, and Technology of Kanazawa University by MEXT (to G.N), MEXT/JSPS KAKENHI grant number 24K18449 (to K.L.), 20H05939 (to Y.O.) and 22H05537, 22H02209, 23H04278 and 24H01276 (to R.W.W.) from MEXT Japan; and by JST CREST Grant Number JPMJCR22E3 (to R.W.W.), and by grants from the Hokuriku Bank grant (to K.L), the Takeda Science Foundation, Japan (to R.W.W.), and the Shimadzu Science Foundation, Japan (to R.W.W.).

Author contributions: Conceptualization: R.W.; Data curation: G.N., A.K., and Y.Q.; Formal analysis G.N., A.K., and Y.Q.; Funding acquisition Y.O. and R.W.; Investigation: G.N., A.K., Y.Q., K.L., M.H., T.A., Y.O., and R.W.; Methodology: G.N.; Project administration: R.W.; Supervision: K.L., Y.O., and R.W; Validation: G.N., A.K., Y.Q., K.L., M.H., T.A., Y.O., and R.W.; Visualization: G.N., A.K., Y.Q., K.L., M.H., T.A., Y.O., and R.W.; Writing—original draft: R.W.; Writing—review & editing: G.N., K.L., Y.O., and R.W.

Supplementary data

Supplementary data is available at NAR online.

Conflict of interest

None declared.

Funding

This work was supported by the World Premier International Research Center Initiative (WPI). This work was also supported by WISE Program for Nano-Precision Medicine, Science, and Technology of Kanazawa University by MEXT (to G.N), MEXT/JSPS KAKENHI grant number 24K18449 (to K.L.), 20H05939 (to Y.O.) and 22H05537, 22H02209, 23H04278 and 24H01276 (to R.W.W.) from MEXT Japan; and by JST CREST Grant Number JPMJCR22E3 (to R.W.W.), and by grants from the Hokuriku Bank grant (to K.L), the Takeda Science Foundation, Japan (to R.W.W.), and the Shimadzu Science Foundation, Japan (to R.W.W.).

Data availability

The data underlying this article will be shared on reasonable request to the corresponding author.

References

1. Okada Y. Sperm chromatin structure: insights from *in vitro* to in situ experiments. *Curr Biol* 2022;**75**:444–51.https://doi.org/10.1016/j.ceb.2022.102075
2. Yamaguchi K, Hada M, Fukuda Y *et al.* Re-evaluating the localization of sperm-retained histones revealed the modification-dependent accumulation in specific genome regions. *Cell Rep* 2018;**23**:3920–32. https://doi.org/10.1016/j.celrep.2018.05.094
3. Jung YH, Sauria MEG, Lyu X *et al.* Chromatin states in mouse sperm correlate with embryonic and adult regulatory landscapes. *Cell Rep* 2017;**18**:1366–82. https://doi.org/10.1016/j.celrep.2017.01.034
4. Balder P, Jones C, Coward K *et al.* Sperm chromatin: evaluation, epigenetic signatures and relevance for embryo development and assisted reproductive technology outcomes. *Eur J Cell Biol* 2024;**103**:151429. https://doi.org/10.1016/j.ejcb.2024.151429
5. Ward WS, Coffey DS. DNA packaging and organization in mammalian spermatozoa: comparison with somatic cells. *Biol Reprod* 1991;**44**:569–74. https://doi.org/10.1095/biolreprod44.4.569
6. McMillan RB, Bediako H, Devenica LM *et al.* Protamine folds DNA into flowers and loop stacks. *Biophys J* 2023;**122**:4288–302. https://doi.org/10.1016/j.bpj.2023.10.003
7. Ukogu OA, Smith AD, Devenica LM *et al.* Protamine loops DNA in multiple steps. *Nucleic Acids Res* 2020;**48**:6108–19. https://doi.org/10.1093/nar/gkaa365
8. Allen MJ, Bradbury EM, Balhorn R. AFM analysis of DNA–protamine complexes bound to mica. *Nucleic Acids Res* 1997;**25**:2221–6. https://doi.org/10.1093/nar/25.11.2221
9. Hud NV, Allen MJ, Downing KH *et al.* Identification of the elemental packing unit of DNA in mammalian sperm cells by atomic force microscopy. *Biochem Biophys Res Commun* 1993;**193**:1347–54. https://doi.org/10.1006/bbrc.1993.1773
10. Brewer LR, Corzett M, Balhorn R. Protamine-induced condensation and decondensation of the same DNA molecule. *Science* 1999;**286**:120–3. https://doi.org/10.1126/science.286.5437.120
11. Yin Q, Yang CH, Strelkova OS *et al.* Revisiting chromatin packaging in mouse sperm. *Genome Res* 2023;**33**:2079–93. https://doi.org/10.1101/gr.277845.123
12. Vara C, Paytuví-Gallart A, Cuartero Y *et al.* Three-dimensional genomic structure and cohesin occupancy correlate with transcriptional activity during spermatogenesis. *Cell Rep* 2019;**28**:352–67. https://doi.org/10.1016/j.celrep.2019.06.037
13. Jung YH, Kremsky I, Gold HB *et al.* Maintenance of CTCF- and transcription factor-mediated interactions from the gametes to the early mouse embryo. *Mol Cell* 2019;**75**:154–71. https://doi.org/10.1016/j.molcel.2019.04.014
14. Ke Y, Xu Y, Chen X *et al.* 3D Chromatin structures of mature gametes and structural reprogramming during mammalian embryogenesis. *Cell* 2017;**170**:367–81. https://doi.org/10.1016/j.cell.2017.06.029
15. Okada Y, Yamaguchi K. Epigenetic modifications and reprogramming in paternal pronucleus: sperm, preimplantation

embryo, and beyond. *Cell Mol Life Sci* 2017;**74**:1957–67. https://doi.org/10.1007/s00018-016-2447-z
16. Okada Y. Sperm chromatin condensation: epigenetic mechanisms to compact the genome and spatiotemporal regulation from inside and outside the nucleus. *Genes Genet Syst* 2022;**97**:41–53. https://doi.org/10.1266/ggs.21-00065
17. Umeda K, McArthur SJ, Kodera N. Spatiotemporal resolution in high-speed atomic force microscopy for studying biological macromolecules in action. *Microscopy (Oxf)* 2023;**72**:151–61. https://doi.org/10.1093/jmicro/dfad011
18. Ando T. Functional implications of dynamic structures of intrinsically disordered proteins revealed by high-speed AFM imaging. *Biomolecules* 2022;**12**:1876. https://doi.org/10.3390/biom12121876
19. Ando T, Fukuda S, Ngo KX *et al.* High-speed atomic force microscopy for filming protein molecules in dynamic action. *Annu Rev Biophys* 2024;**53**:19–39. https://doi.org/10.1146/annurev-biophys-030722-113353
20. Mohamed MS, Hazawa M, Kobayashi A *et al.* Spatiotemporally tracking of nano-biofilaments inside the nuclear pore complex core. *Biomaterials* 2020;**256**:120198. https://doi.org/10.1016/j.biomaterials.2020.120198
21. Mohamed MS, Kobayashi A, Taoka A *et al.* High-speed atomic force microscopy reveals loss of nuclear pore resilience as a dying code in colorectal cancer cells. *ACS Nano* 2017;**11**:5567–78. https://doi.org/10.1021/acsnano.7b00906
22. Qiu Y, Sajidah ES, Kondo S *et al.* An efficient method for isolating and purifying nuclei from mice brain for single-molecule imaging using high-speed atomic force microscopy. *Cells* 2024;**13**:279. https://doi.org/10.3390/cells13030279
23. Sajidah ES, Lim K, Yamano T *et al.* Spatiotemporal tracking of small extracellular vesicle nanotopology in response to physicochemical stresses revealed by HS-AFM. *J Extracell Vesicles* 2022;**11**:e12275. https://doi.org/10.1002/jev2.12275
24. Lim K, Nishide G, Sajidah ES *et al.* Nanoscopic assessment of anti-SARS-CoV-2 spike neutralizing antibody using high-speed AFM. *Nano Lett* 2023;**23**:619–28. https://doi.org/10.1021/acs.nanolett.2c04270
25. Lim K, Nishide G, Yoshida T *et al.* Millisecond dynamic of SARS-CoV-2 spike and its interaction with ACE2 receptor and small extracellular vesicles. *J Extracell Vesicles* 2021;**10**:e12170. https://doi.org/10.1002/jev2.12170
26. Lim KS, Mohamed MS, Wang H *et al.* Direct visualization of avian influenza H5N1 hemagglutinin precursor and its conformational change by high-speed atomic force microscopy. *Biochim Biophys Acta* 2020;**1864**:129313. https://doi.org/10.1016/j.bbagen.2019.02.015
27. Nishide G, Lim K, Tamura M *et al.* Nanoscopic elucidation of spontaneous self-assembly of severe acute Respiratory syndrome coronavirus 2 (SARS-CoV-2) open reading frame 6 (ORF6) protein. *J Phys Chem Lett* 2023;**14**:8385–96. https://doi.org/10.1021/acs.jpclett.3c01440
28. Nishide G, Lim K, Mohamed MS *et al.* High-speed atomic force microscopy reveals spatiotemporal dynamics of histone protein H2A involution by DNA inchworming. *J Phys Chem Lett* 2021;**12**:3837–46. https://doi.org/10.1021/acs.jpclett.1c00697
29. Allen MJ, Lee C, Lee JDt *et al.* Atomic force microscopy of mammalian sperm chromatin. *Chromosoma* 1993;**102**:623–30. https://doi.org/10.1007/BF00352310
30. Tongu C, Kenmotsu T, Yoshikawa Y *et al.* Divalent cation shrinks DNA but inhibits its compaction with trivalent cation. *J Chem Phys* 2016;**144**:205101. https://doi.org/10.1063/1.4950749
31. Maeshima K, Matsuda T, Shindo Y *et al.* A transient rise in free Mg(2+) ions released from ATP-Mg hydrolysis contributes to mitotic chromosome condensation. *Curr Biol* 2018;**28**:444–51. https://doi.org/10.1016/j.cub.2017.12.035

Received: September 12, 2024. **Revised:** February 6, 2025. **Editorial Decision:** February 11, 2025. **Accepted:** February 21, 2025